Modeling of a dispersive tsunami caused by a submarine landslide based on detailed bathymetry of the continental slope in the Nankai trough, southwest Japan

Toshitaka Baba[a], Yodai Gon[a], Kentaro Imai[b], Kei Yamashita[c], Tetsuo Matsuno[d], Mitsuru Hayashi[e], Hiroshi Ichihara[f]

[a]Graduate School of Technology, Industrial and Social Sciences, Tokushima University, 2-1 Minami-jyosanjima-cho, Tokushima 770-8506, Japan
[b]Research and Development Center for Earthquake and Tsunami Japan Agency for Marine-Earth Science and Technology, 3173-25 Showa-machi, Kanazawa, Yokohama, 236-0001, Japan
[c]International Research Institute of Disaster Science, Tohoku University, 468-1 Aoba, Aramaki, Aoba-ku, Sendai 980-8572, Japan
[d]Kobe Ocean-Bottom Exploration Center, Kobe University 5-1-1 Fukaeminami, Higashinada-ku Kobe 658-0022, Japan
[e]Research Center for Inland Seas, Kobe University, 5-1-1 Fukaeminami, Higashinada-ku Kobe 658-0022, Japan
[e]Earthquake and Volcano Research Center, Graduate School of Environmental Studies, Nagoya University, Furo-cho, Chikusa-ku, Nagoya 464-8601, Japan

Correspondence to
Toshitaka Baba
e-mail: baba.toshi@tokushima-u.ac.jp

Manuscript on 22/01/2019 to be submitted for Tectonophysics
Revised on 04/07/2019

Highlights

- Bathymetric survey shows detailed features of the submarine landslide
- Two-layer flow model estimates the submarine mass movement
- Tsunamis caused by the submarine landslide are deeply affected by dispersion effects

Abstract

Tsunamis caused by submarine landslides are not accompanied by seismic waves and thus may appear at the coast without warning. In this study, detailed bathymetric surveys with a multi-narrow beam echo sounder were used to map submarine landslides on the continental shelf near Cape Muroto, in the Nankai trough off southwestern Japan. One of the surveyed submarine landslides was selected to supply dimensions for the simulation of a submarine mass movement by a two-layer flow model in which the upper and lower layers correspond to seawater and turbidity currents, respectively. The time series of seafloor deformation during this simulated landslide was used as the boundary condition to drive a tsunami simulation. The results showed strong directivity effects during tsunami generation in which pushing-dominant (positive) tsunami waves propagated seaward, in the direction of the submarine landslide, and pulling-dominant (negative) tsunami waves propagated landward. Both types of waves were strongly modified by frequency dispersion. For pulling-dominant waves, a tsunami simulation that included dispersion (Boussinesq) terms predicted greater maximum tsunami heights than a non-dispersive tsunami simulation. To avoid underestimation of tsunami heights, we recommend including dispersion terms when modeling tsunamis caused by submarine landslides for disaster planning purposes.

Keywords: Tsunami, Submarine landslide, Directivity, Dispersion, Nankai trough

1. Introduction

Tsunamis are caused by vertical displacement of the seafloor, which occurs not only from earthquakes, but also from submarine landslides. Earthquake-induced submarine landslides amplified tsunamis from the 1998 Papua New Guinea earthquake (Tappin et al., 2001, 2008), a moderate earthquake in Suruga Bay, Japan, in 2009 (Baba et al., 2012; Matsumoto et al., 2012), and the 2010 Haiti earthquake (Hornbach et al., 2010). In these cases, the causative submarine landslides were identified by surveys and validated by numerical simulations. The great tsunami of the 2011 Tohoku earthquake may likewise have been affected by a submarine landslide near the trench (Fujiwara et al., 2011, Tappin et al., 2014), and the tsunami caused by the 2018 Palu earthquake may have been amplified by submarine landslides (Arikawa et al., 2018, Muhari et al., 2018, Sassa and Takagawa, 2018). Some historical large tsunamis may have originated from submarine landslides (e.g. Matsumoto and Kimura, 1993; Yanagisawa et al., 2016). Submarine landslides generally do not radiate a clear seismic signal, thus the tsunamis they cause may arrive at the coast without warning. Accordingly, submarine landslides may be the origin of tsunamis that have been attributed to tsunami earthquakes (Kanamori, 1972). However, risk assessments of submarine landslide tsunamis are difficult to make without detailed knowledge of the physics of submarine landslides and the interactions between these mass movements and water bodies.

In contrast, many submarine landslides around the world have been well characterized by detailed bathymetric surveys, visual observations, seismic images, and drill cores (e.g., Haflidason et al., 2005;

Masson et al., 2006; Cardona et al., 2016). Submarine landslides have been mapped in detail in the Nankai trough, Japan, a subduction zone where many historical earthquakes and tsunamis have been recorded.

Bathymetric data from the forearc slope of the Nankai trough, where splay faults branch from the plate boundary, reveal the scarps of many seafloor slumps (Kimura et al., 2011). These slumps occur on slopes of ~4° and their headscarps dip at angles of ~6–8°, suggesting that the slope is at or near the critical angle, and that slight tilting or shaking could trigger slope failures. Kawamura et al. (2012) used a remotely operated vehicle to visually observe three submarine slump scarps at the toe of the Nankai accretionary prism, and estimated that they displaced volumes of 3.3, 30.6, and 11.3 km^3, respectively.

Strasser et al. (2011, 2012) used drill cores and 2D seismic images to detect six buried mass-transport deposits ranging in thickness from 0.5 to 61 m in the Kumano basin of the Nankai accretionary wedge. The oldest of these was deposited between 0.85 and 1.05 Ma. Moore and Stasser (2016) used 3D seismic data to investigate surficial and buried submarine landslides in a 15 × 15 km area in the slope basin. They described two surficial landslides, one of them a rotational slump ~3.4 km wide, 1.8 km long, and 150 m thick and the other a disintegrative slide that left a seafloor scar more than 3.65 km wide, 2.6 km long, and ~200m deep. They estimated the recurrence interval for submarine landslides to be 500–1000 years, far longer than the 100–200 year recurrence interval for great earthquakes in the Nankai trough (Ando 1975; Ishibashi and Satake, 1998).

The continental slope closer to shore also has many scarps created by submarine landslides. On the continental slope off southwestern Japan, clear slump scarps have been documented about 25 km from the coast (Moriki et al., 2017). These represent slump events that could have caused tsunamis, but the associated submarine landslides and their tsunami potential have not been investigated. To assess the risk of tsunamis from these submarine landslides, we carried out a bathymetric survey to reveal their detailed features, and we modeled the tsunamis they might have caused. In the tsunami calculations, dispersive equations were used because the tsunami sources caused by submarine landslides are smaller than the application limit of the long-wave theory.

2. Bathymetric survey

Multi-narrow beam bathymetric surveys were carried out about 25 km east of Cape Muroto on Shioku Island, southwestern Japan, by training ship (TS) *Fukae-maru* belonging to Kobe University (Fig. 1a). The ship's multi-narrow beam echo sounder (EM 712, Kongsberg Maritime) acquired bathymetric data in the study area during research cruises on 25–26 August 2017, 18 March 2018 and 29–30 August 2018. The ship's speed was maintained at 8 knots during the bathymetric surveys to reduce noise derived from the ship's movements and to acquire high-resolution data while covering large survey areas. Sound speed corrections were made from expendable conductivity/temperature/depth probe observations during each cruise. By using HIPS and SHIPS 11.0 software to process the data, we obtained bathymetric data with a resolution of about 50 m.

The resulting bathymetric map shows four sets of headscarps representing slumps, named A to D, on the continental slope (Fig. 1b and Table 1). The largest of these, slump B, is about 4.2 km long with a headscarp about 6.9 km wide, and extends from a depth of about 640 m to about 1,340 m at an average slope angle of about 5°. The seafloor topography suggests that slump D was a single collapse and that slumps B and C were multiple slope collapses; however, none of these have clearly defined slump

deposits below their toes. Conversely, for slump A, the slope below the headscarp is smooth and slump deposits are evident on the slope below. We therefore interpret slumps B, C, and D as being old, and slump A as being relatively young.

Figure 2 shows bathymetric profiles of the four slumps compared to profile Z, which crosses the continental slope at a nearby location without a slump. Although the depths of the headscarps differ among the profiles, their angles and slopes are similar. The thicknesses of slump bodies were estimated from the vertical difference between the slump profiles and profile Z, which permitted estimation of the slump volumes.

Small, closely spaced gullies are ubiquitous on the seafloor slopes. The distribution density of the gullies is 1.36–2.63 gully/km, the distance between the gullies ranges from about 380 to 730 m, and the gullies range in depth from about 10 to 50 m. Gullies are especially well developed on submarine slumps B, C, and D, where they deeply incise the headscarps and slopes.

3. Modeling mass movement of a submarine slump

Several methods have been used to calculate the initial conditions of tsunamis caused by submarine landslides. Satake (2007) used the difference in seafloor topography before and after the slide to estimate the size of the sliding mass and assumed a velocity for that mass to model the development of seafloor deformation during the slide. The resulting time series of seafloor deformation was then used to drive the sea surface in a one-layer flow tsunami simulation. Watts et al. (2005) proposed an empirical equation to obtain tsunami initial conditions from theoretical and experimental investigations. Imamura and Imteaz (1995) modeled tsunamis with a scheme of two coupled layers corresponding to seawater and a turbidity current.

The bathymetric map displays a definite slump deposit below slump A, but none below slumps B, C, and D. No large fragments derived from the slump mass were found below any of the four slumps. These observations mean that the slump bodies may have disintegrated into turbidity currents that travelled far into the deep ocean. The well-developed gullies indicate that the seafloor in the study area is covered by relatively weak sediment, which would tend to generate turbidity currents rather than block movements. For these reasons, we adopted the two-layer flow model of Imamura and Imteaz (1995) to simulate the movement of the submarine mass.

The two-layer flow model was derived from the two Euler equations for the upper and lower layers using a long wave approximation and shear stress (friction) on the interface between the two layers. Flow velocities were integrated in the vertical direction in each layer. Zero hydrostatic pressure was assumed as the boundary condition at the surface of the upper layer, and the hydrostatic pressure calculated from the thickness of the upper layer was taken for the interface between the layers. The governing equations are (Imamura and Imteaz, 1995):

$$\frac{\partial M_1}{\partial x} + \frac{\partial N_1}{\partial y} + \frac{\partial}{\partial t}(\eta_1 - \eta_2) = 0 \tag{1}$$

$$\frac{\partial M_1}{\partial t} + \frac{\partial (M_1^2/D_1)}{\partial x} + \frac{\partial (M_1 N_1/D_1)}{\partial y} + gD_1 \frac{\partial \eta_1}{\partial x} - INTF = 0 \tag{2}$$

$$\frac{\partial N_1}{\partial t} + \frac{\partial (M_1 N_1/D_1)}{\partial x} + \frac{\partial (N_1^2/D_1)}{\partial y} + gD_1 \frac{\partial \eta_1}{\partial y} - INTF = 0 \tag{3}$$

$$\frac{\partial M_2}{\partial x} + \frac{\partial N_2}{\partial y} + \frac{\partial \eta_2}{\partial t} = 0 \tag{4}$$

$$\frac{\partial M_2}{\partial t}+\frac{\partial (M_2^2/D_2)}{\partial x}+\frac{\partial (M_2N_2/D_2)}{\partial y}+gD_2\left\{\alpha\left(\frac{\partial \eta_1}{\partial x}+\frac{\partial h_1}{\partial x}-\frac{\partial \eta_2}{\partial x}\right)+\frac{\partial \eta_2}{\partial x}-\frac{\partial h_1}{\partial x}\right\} + \frac{gn^2}{{D_2}^{7/3}}M_2\sqrt{{M_2}^2+{N_2}^2}+INTF=0 \quad (5)$$

$$\frac{\partial N_2}{\partial t}+\frac{\partial (M_2N_2/D_2)}{\partial x}+\frac{\partial (M_2^2/D_2)}{\partial y}+gD_2\left\{\alpha\left(\frac{\partial \eta_1}{\partial y}+\frac{\partial h_1}{\partial y}-\frac{\partial \eta_2}{\partial y}\right)+\frac{\partial \eta_2}{\partial y}-\frac{\partial h_1}{\partial y}\right\} + \frac{gn^2}{{D_2}^{7/3}}N_2\sqrt{{M_2}^2+{N_2}^2}+INTF=0 \quad (6)$$

where subscripts 1 and 2 indicate the upper and lower layers, respectively, η is the surface elevation, M and N are discharge along the x and y axis, respectively, ρ is the fluid density, α is the relative density ratio (ρ_1/ρ_2 = 1.00/1.65), h is the static water depth, $D=h+\eta$ is the total water depth, and g is the acceleration due to gravity. See Fig. 3a for a schematic representation of these terms. The interfacial shear stress $INTF$ is defined by $f_{inter}\bar{u}|\bar{u}|$, where $\bar{u}$ is the velocity of the lower layer with respect to the upper layer and f_{inter} is the interfacial drag coefficient. Equations (5) and (6) include a bottom friction term in which n is Manning's roughness coefficient. Values of 0.2 for f_{inter} and 0.08 $sm^{-1/3}$ for n were used in this study, as determined by laboratory experiments (Kawamata et al., 2005; McLeod et al., 1997) and numerical studies (Maeno and Imamura, 2007, 2011). Equations (1) and (4) are the equations of continuity for the upper and lower layers, respectively. Equations from (2) and (3) are the equations of motion for the upper layer and equations (5) and (6) are those for the lower layers.

To model the initial condition of the slump mass, we chose slump A because it was geometrically simple and its slump deposit was well preserved. Using the parameters of slump A in Table 1, we adopted a cylindrical slump body with a diameter of 4.2 km and a height of 210 m. The cylinder edges were tapered by a cosine curve toward the outside to avoid abrupt accelerations around the slump body. The slump body was positioned within the present (i.e., post-slump) bathymetry at the location of slump A. This slump body corresponds to the high-density lower layer in the two-layer flow model.

The computations adopted a staggered-grid, leap-frog finite differential scheme in Cartesian coordinates, and the computational domain was defined as shown in Fig. 4. The regional bathymetric grid was derived from data compiled by the Japanese cabinet office for the preparation of tsunami hazard maps for the Nankai great earthquake scenario (Geospatial Information Center, 2018). The spatial interval of the computational grid was set at 90 m, and the time interval of the computation was set at 0.1 s to substantially satisfy the stability condition. The movement of the submarine mass from slump A was calculated for 1 hour after the collapse.

Figure 5 shows the submarine mass movement obtained from the two-layer simulation. The collapse progresses down slope in the southeastern direction. The phase velocity of the submarine mass movement is approximately 21 m/s, because the main collapse is finished by about 200 s for the slump body with a length of 4.2 km. The maximum flow velocity of the lower layer is 19.35 m/s in the simulation. The displaced mass continues to spread out over a wide area, as far as 30 km from its origin, by the end of the simulation.

4. Tsunami simulations

For our tsunami calculations, we adopted a one-layer shallow water model using JAGURS tsunami simulation software (Baba et al., 2015, 2017) parallelized by OpenMP and MPI. JAGURS solves the following shallow water equations without dispersion (Boussinesq) terms (Eqs. (7)–(9)) or with them

(Eqs. (7), (10), and (11)) in a staggered-grid, leap-frog finite differential scheme (See Fig. 3b for notation):

$$\frac{\partial M}{\partial x}+\frac{\partial N}{\partial y}+\frac{\partial \eta}{\partial t}=0 \tag{7}$$

$$\frac{\partial M}{\partial t}+\frac{\partial (M^2/D)}{\partial x}+\frac{\partial (MN/D)}{\partial y}+gD\frac{\partial \eta}{\partial x}+\frac{gn^2}{D^{7/3}}M\sqrt{M^2+N^2}=0 \tag{8}$$

$$\frac{\partial N}{\partial t}+\frac{\partial (MN/D)}{\partial x}+\frac{\partial (N^2/D)}{\partial y}+gD\frac{\partial \eta}{\partial y}+\frac{gn^2}{D^{7/3}}N\sqrt{M^2+N^2}=0 \tag{9}$$

$$\frac{\partial M}{\partial t}+\frac{\partial (M^2/D)}{\partial x}+\frac{\partial (MN/D)}{\partial y}+gD\frac{\partial \eta}{\partial x}+\frac{gn^2}{D^{7/3}}M\sqrt{M^2+N^2}-\frac{h^2}{3}\frac{\partial}{\partial x}\left(\frac{\partial^2 M}{\partial x\partial t}+\frac{\partial^2 N}{\partial y\partial t}\right)=0 \tag{10}$$

$$\frac{\partial N}{\partial t}+\frac{\partial (MN/D)}{\partial x}+\frac{\partial (N^2/D)}{\partial y}+gD\frac{\partial \eta}{\partial y}+\frac{gn^2}{D^{7/3}}N\sqrt{M^2+N^2}-\frac{h^2}{3}\frac{\partial}{\partial y}\left(\frac{\partial^2 M}{\partial x\partial t}+\frac{\partial^2 N}{\partial y\partial t}\right)=0 \tag{11}$$

$$\Delta\eta_0(x,y)=\frac{1}{(2\pi)^2}\int_{-\infty}^{\infty}\int_{-\infty}^{\infty}dk_x dk_y e^{i(k_x x+k_y y)}\frac{\widetilde{\Delta\eta_2}(k_x,k_y)}{\cosh kh_{ave}} \tag{12}$$

$$\eta=\eta^*+\Delta\eta_0 \tag{13}$$

To improve the stability of calculations, the advection terms were only calculated using the first-order upwind difference. The dispersion terms, i.e., the last terms on the left-hand side of equations (10) and (11), were solved by an implicit (Gauss-Seidel) method.

Equation (12) is the full potential method of Kajiura (1963) that we used to calculate increments of the vertical displacement of the sea surface resulting from the submarine mass movement (Fig. 5) imposed on the seafloor. In this equation, $\Delta\eta_0$ and $\Delta\eta_2$ are increments of vertical displacement at the sea surface and seafloor, respectively, at each time step. $\Delta\eta_2$ was calculated from η_2 of equation (4), and $\widetilde{\Delta\eta_2}$ is the Fourier transform of $\Delta\eta_2$. h_{ave} is the average water depth at the tsunami source, k is the wave number, and i is the imaginary unit. η^* in equation (13) is the temporary sea surface fluctuation obtained by equation (7) before the tsunami generated by movement of the lower layer is added. As the tsunami propagates, calculated increments of vertical displacement at the sea surface ($\Delta\eta_0$) are sequentially added to the temporary sea surface fluctuation (η^*) at each time step. We refer to this scheme as the time-dependent input in this study.

We note that the time-dependent input to the 2D tsunami simulation cannot accurately simulate the pressure field during tsunami generation because it neglects dynamic pressure effects. However, in areas outside the tsunami-generating region, tsunami wavefields can be correctly simulated by the time-dependent input. Saito (2013, 2019) investigated analytical solutions for 3D tsunami generation over a flat seafloor. Saito (2013) concluded that "in order to properly include the tsunami generation process in the initial tsunami height distribution for 2D tsunami simulations, only the effect of the water height distribution (the first term in Eq. (32)) is taken into account at each time step of the tsunami simulation. We should not add the velocity distribution generated from the source." Furthermore, Lotto et al. (2017) carried out full 3D simulations that included the effects of earthquake faulting and tsunami generation and propagation over non-flat seafloors. In their simulations, depth-dependent horizontal and vertical velocity fields appeared during the tsunami generation phase, but these velocity fluctuations did not

propagate outside the tsunami source area. Accordingly, we assumed an initial velocity distribution of zero in our simulation to predict tsunamis in areas outside of their source region. Given these considerations, the time-dependent input method used in this study is appropriate to simulate tsunamis.

The tsunami propagations were calculated by JAGURS both without dispersion terms (Fig. 6) and with dispersion terms (Fig. 7). The computations used the same bathymetric data and computational domain (Fig. 4) used in the two-layer flow model. A sponge buffer zone (Cerjan et al., 1985) was applied to grid cells within 20 cells of the edge of the computational domain to avoid reflections of tsunami waves. A uniform Manning's roughness coefficient of 0.025 $sm^{-1/3}$ was used for the whole computation region. Again, the simulations used a time step of 0.1 s and ran for 1 hour.

In both calculations, generation of the tsunami by the submarine slump is finished by about 200 s. Both simulations also feature a pushing (positive) tsunami wave moving seaward and a pulling (negative) tsunami wave moving landward. This asymmetry in tsunami propagation, which we refer to here as directivity, reflects the fact that the submarine mass moves downslope with a velocity comparable to the tsunami phase velocity (Fig. 5). According to Watada (2013), the phase velocity of the turbidity current in the two-layer flow model is predicted to be about 25 m/s assuming h_1 = 790 m, h_2 = 210 m, and ρ_1/ρ_2 = 1.00/1.65. For its parts, the tsunami phase velocity (c) can be written as:

$$c = \sqrt{\frac{gL}{2\pi}\tanh\left(\frac{2\pi h}{L}\right)} \tag{14}$$

where L is the tsunami wavelength. Equation (14) predicts a phase velocity of about 88 m/s, assuming h = 790 m for a long wave. For a dispersive wave, equation (14) predicts a phase velocity of about 74 m/s, assuming h = 790 m and L = 4,200 m. Accordingly, the dispersive tsunami calculations yield stronger directivity effects than the non-dispersive calculations. The difference in the directivity is apparent in a comparison between the images at 60 s of Fig. 6 and 7 during the tsunami generation process. The distributions of simulated maximum water levels are also different (Fig. 8).

The left-hand panels (a, c and e) in Figure 9 show clear differences between tsunami waveforms calculated by non-dispersive and dispersive modeling. Dispersive wave trains are clearly evident in the first pulling wave, in the images after 180 s in Figure 7 and in the waveform shown in blue in Figures 9c and 9e, but are absent in the non-dispersive simulation (Fig. 6 and the red waveform in Figs. 9c and 9e).

5. Discussion

5.1 Comparison of tsunamis from time-dependent and static inputs

Because it is so difficult to directly observe dynamic mass movements in the deep sea, submarine mass movements are usually recognized by the difference in water depths before and after the collapse. Therefore, we performed substitute tsunami calculations in which the time-dependent input was replaced with a static input based on changes in water depths. The depth change at 3,600 s, in the last panel of Figure 5, was used as the static input. We applied the full potential method of Kajiura (1963) to this static input to estimate the initial sea surface condition. We assumed a rise time of 200 s for the initial sea surface condition according to the result of the two-layer model because instantaneous tsunami generation is not realistic for a submarine landslide tsunami. The rest of the simulations were unchanged from those made with the time-dependent input. Dispersive and non-dispersive equations were solved to obtain tsunami waveforms at the imaginary gauges shown in Figure 8.

The tsunami waveforms calculated with the static input are presented in the right-hand panels (b, d and f) of Figure 9. These differ from those produced with the time-dependent input (Figs. 9a, 9c and 9e) in terms of the maximum sea surface rise and fall, dominant period, and arrival time. In particular, the difference between dispersive (blue) and non-dispersive (red) waveforms is smaller in the results based on the static input. This is because the static input generates a tsunami with a longer wavelength than the time-dependent input.

5.2 Importance of dispersion in submarine landslide tsunami predictions

For the time-dependent input, it is interesting that near the coast, the dispersive model predicted greater maximum tsunami heights than the non-dispersive model (Fig. 8). Frequency dispersion, by spreading out the wave train, usually results in smaller maximum tsunami heights for the case of a pushing-dominant wave as shown in the waveform of Figure 9a. However, for the case of pulling dominant waves, dispersion has the opposite effect on the tsunami waveforms, increasing the maximum tsunami height as shown in the waveform of Figure 9c and 9e. Our model couples the two factors of directivity and dispersion to produce a higher tsunami near the coast in Figure 8.

Although tsunamis are also dispersive water waves, the effect of dispersion is often neglected when creating tsunami hazard maps for earthquake-generated tsunamis. This is because the spatial dimensions of the earthquake-generated tsunamis are much greater than the water depth, such that dispersive effects are generally small. Dispersion is neglected, too, because of the difficulties of dispersive tsunami calculations, which include high computational costs and the occurrence of numerical instabilities resulting from the higher derivatives in space and time. The final and the most important reason is that the non-dispersive calculations tend to predict higher tsunamis than dispersive calculations, as shown in the waveform of Figure 9a. Although the non-dispersive model may overpredict the maximum tsunami height, this conservative approach is acceptable for disaster management agencies tasked with safeguarding lives and properties.

However, the spatial dimensions of submarine landslide tsunamis are smaller than those of earthquake-generated tsunamis, such that the effects of dispersion may be significant. Moreover, the strong directivity of effects related to submarine mass movements means that short-wavelength pulling-dominant waves are typically directed landward and are amplified as an effect of frequency dispersion. Accordingly, we strongly recommend using dispersive equations when modeling submarine landslide tsunamis not only for accuracy but also for safety-related purposes.

5.3. Risk assessment of submarine landslide tsunamis

The magnitude of a tsunami caused by a submarine landslide is determined by the volume of the landslide mass and its velocity. If a submarine mass movement is much slower than the phase velocity of a tsunami, it cannot generate a tsunami. The two-layer flow model used in this study assumes that there is no internal friction in the turbidity layer and thus predicts a high sliding velocity, which in turn imposes a strong directivity on the tsunami and reinforces its amplitude. Our assumption of no internal friction in this study is supported by the widespread deposit of slump sediment below the toe of slump A and by the presence of well-developed gullies on the seafloor, implying that the seafloor sediments are weak in the study area (Fig. 1b). Furthermore, an outcrop study has shown that earthquake-induced liquefaction reduces sediments' shear strength such that the submarine landslide mass moves at high speed (Yamamoto and Kawakami, 2014), with relativety small or negligible internal

303 friction.

304 Our detailed bathymetric map clearly shows that the continental slope has collapsed multiple times
305 and in multiple places. The overlapping configuration of submarine slumps A to D implies that they
306 collapsed as a series, the initial slump creating unstable slopes along its side scarps, which then led to
307 new failures in adjacent areas. Lateral migration of submarine landslides has been documented by
308 Yamamoto and Kawakami (2014), who identified at least five discrete failure masses with laterally
309 varying ages along the strike of the trough axis in the trench-slope basin sediments of the Chikura
310 Group in the Boso Peninsula. Similarly, an analog study (Yamada et al., 2010) also identified systematic
311 patterns of lateral migration of intermittent slope failures to adjacent locations. In conclusion, the
312 possibility of future collapses that would generate tsunamis should be a concern in the area of this
313 study.
314
315 **6. Conclusions**

316 Bathymetric surveys by TS *Fukae-maru* revealed details of four submarine landslides, here referred
317 to as A though D, about 25 km to the east of Cape Muroto, in the Nankai trough (Fig. 1). Their
318 headscarps are adjacent to each other on the continental slope at water depths between about 640 and
319 860 m, and their displaced volumes range from 0.4 to 4.8 km^3. Slumps B through D are interpreted to
320 be relatively old based on evidence of deep gully incisions, multiple collapses, and the absence of
321 debris deposits below their toes. Submarine slump A, in contrast, is less incised by gullies, seems to
322 represent a single collapse, and has an intact debris deposit at its toe. The dimensions of this youthful
323 slump (Table 1) were used as input for simulations of a submarine landslide and the resulting tsunami.

324 The submarine slump was simulated with a two-layer flow model in which the upper layer is seawater
325 and the lower layer treats the sediment of the slump as a turbidity current. The simulated collapse
326 progresses at high speed down the seafloor slope and leaves widespread deposits as far as 30 km from
327 the origin after 1 hour of simulation time. The movement of this simulated slump was then applied to
328 the seafloor as a boundary condition for the tsunami simulation. The tsunami calculations used a
329 conventional one-layer shallow water model in JAGURS tsunami simulation software. The high-
330 velocity submarine mass movement is effective in generating a tsunami with strong directivity because
331 its motion is comparable to the tsunami phase velocity. A pushing (positive) tsunami wave propagates
332 seaward and a pulling (negative) wave propagates landward.

333 We also investigated the effects of dispersion on the modeled tsunami by solving the shallow water
334 equations with and without dispersion (Boussinesq) terms. Dispersion has a clear effect on the tsunamis
335 caused by submarine slumping because they arise from a small source and have small spatial
336 dimensions. For short-wavelength tsunamis with pulling-dominant waves, the maximum tsunami height
337 is amplified by the frequency dispersion. Accordingly, we strongly recommend the use of dispersive
338 equations to avoid underestimating the height of tsunamis caused by submarine landslides.
339
340 **Acknowledgements**

341 We deeply thank the captain, crews, researchers who served on the cruises of TS *Fukae-maru* cruises.
342 Discussions of the tsunami generation process with Dr. Tatsuhiko Saito were very fruitful. We thank
343 four anonymous reviewers and the editors, Dr. Kelin Wang, Dr. Eiichi Fukuyama, and Dr. Phil R.
344 Cummins, whose constructive comments improved the manuscript. This study was supported by Japan
345 Society for the Promotion of Science KAKENHI Grants JP15H05718, JP15K21682 and JP19H02409

and CHUBU ELECTRIC POWER CO. INC.

References

Ando, M., 1975, Source mechanisms and tectonic significance of historical earthquake along the Nankai tough, Japan, Tectonophysics, 27, 119–140.

Arikawa, T., A. Muhari, Y. Okumura, Y. Dohi, B. Afriyanto, K.A. Sujatmiko, and F. Imamura, 2018, Coastal subsidence induced several tsunamis during the 2018 Sulawesi earthquake, J. Disaster Res., 13, sc20181204.

Baba, T., H. Matsumoto, K. Kashiwase, T. Hyakudome, Y. Kaneda, and M. Sano, 2012, Micro-bathymetric Evidence for the Effect of Submarine Mass Movement on Tsunami Generation During the 2009 Suruga Bay Earthquake, Japan, in Submarine mass movements and their consequences edited by Y. Yamada et al., Advances in Natural and Technological Hazards Research, 31, pp.485-495.

Baba, T., N. Takahashi, Y. Kaneda, K. Ando, D. Matsuoka, and T. Kato, 2015, Parallel implementation of dispersive tsunami wave modeling with a nesting algorithm for the 2011 Tohoku tsunami, Pure appl. Geophys., 172, 3455–3472, doi:10.1007/s00024-015-1049-2.

Baba, T., S. Allgeyer, J. Hossen, P.R. Cummins, H. Tsushima, K. Imai, K.Yamashita, and T. Kato, 2017, Accurate numerical simulation of the far-field tsunami caused by the 2011 Tohoku earthquake, including the effects of Boussinesq dispersion, seawater density stratification, elastic loading, and gravitational potential change, Ocean Modelling, 111, 46-54, doi:10.1016/j.ocemod.2017.01.002.

Bird, P., 2003, An updated digital model of plate boundaries, Geochemistry Geophysics Geosystems, 4(3), 1027, doi:10.1029/2001GC000252.

Cardona, S. L.J. Wood, R.J. Day-Stirrat, and L. Moscardelli, 2016, Fabric development and pore-throat reduction in a mass-transport deposit in the Jubilee gas field, rastern Gulf of Mexico: Consequences for the sealing capacity of MTDs, Advances in Natural and Technological Hazards Research, 41, in Submarine Mass Movements and their Consequences, edited by G. Lamarche et al., doi:10.1007/978-3-319-20979-1_3.

Cerjan, C., D. Kosloff, R. Kosloff, and M. Reshef, 1985, A nonreflecting boundary condition for discrete acoustic and elastic wave equations, Geophysics, 50, 705–708, doi:10.1190/1.1441945.

Fujiwara T., S. Kodaira, T. No, Y. Kaiho, N. Takahashi, Y. Kaneda, 2011, The 2011 Tohoku-Oki earthquake: Displacement reaching the trench axis, Science, 334, 1240-1240, doi:10.1126/science.1211554.

Geospatial information center, https://www.geospatial.jp/gp_front/, last accessed on 12.12.2018.

Haflidason, H., R. Lien, H.P. Sejrup, C.G. Forsberg, and P. Bryn, 2005, The dating and morphometry of the Storegga Slide. Marine and Petroleum, Geology, 22, 123–136, doi:http://dx.doi.org/10.1016/j.marpetgeo.2004.10.008.

Hornbach, M.J., Nicole Braudy, R.W. Briggs, M. Cormier, M.B. Davis, J.B. Diebold, N. Dieudonne, R. Douilly, C. Frohlich, S.P.S. Gulick, H.E. Johnson III, P. Mann, C. McHugh, K.R. Mishkin, C.S. Prentice, L. Seeber, C.C. Sorlien, M.S. Steckler, S.J. Symithe, F.W. Taylor and J. Templeton, 2010, High tsunami frequency as a result of combined strike-slip faulting and coastal landslides, Nature Geoscience, 3, 783-788, doi:10.1038/NGEO975.

Imamura, F. and M.M.A. Imteaz, 1995, Long waves in two-layers: Governing equations and numerical model, Journal of Science of Tsunami Hazards, 13, 3-24.

Ishibashi K. and K. Satake, 1998, Problems on forecasting great earthquakes in the subduction zones around Japan by means of paleoseismology, Zisin 2, 50, 1–21 (in Japanese).

391 Kajiura, K., 1963, The leading wave of a tsunami, Bull. Earthquake Res., Inst. Univ. Tokyo, 41, 535–
392 571.
393 Kanamori, H., 1972, Mechanism of tsunami earthquake, Phys. Earth Planet. Inter., 6, 346-359.
394 Kawamata, K., K. Takaoka, K. Ban, F. Imamura, S. Yamaki, and E. Kobayashi, 2005, Model of tsunami
395 generation by collapse of volcanic eruption:The 1741 Oshima‐Oshima tsunami, in Tsunamis: Case
396 Studies and Recent Development, edited by K. Satake, 79–96, Springer, New York.
397 Kawamura, K., A. Sakaguchi, M. Strasser, R. Anma, and H. Ikeda, 2012, Detailed observation of
398 topography and geologic architecture of a submarine landside in a toe of an accretionary prism,
399 Submarine mass movements and their consequences, Advances in Natural and Technological
400 Hazards Research, 31, 301-310.
401 Kimura, G., G.F. Moore, M. Strasser, E. Screaton, D. Curewitz, C. Streiff, and H. Tobin, 2011, Spatial
402 and temporal evolution of the megasplay fault in the Nankai Trough, Geochemistry Geophysics,
403 Geosystem, 12, doi:10.1029/2010GC003335.
404 Lotto, G.C., G. Nava, E.M. Dunham, 2017, Should tsunami simulations include a nonzero initial
405 horizontal velocity?, Earth Planets Space, 69, 117, doi:10.1186/s40623-017-0701-8.
406 Maeno, F., and F. Imamura, 2007, Numerical investigations of tsunamis generated by pyroclastic flows
407 from the Kikai caldera, Japan, Geophys. Res. Lett., 34, L23303, doi:10.1029/2007GL031222.
408 Maeno, F., and F. Imamura, 2011, Tsunami generation by a rapid entrance of pyroclastic flow into the
409 sea during the 1883 Krakatau eruption, Indonesia, J. Geophys. Res., 116, B09205,
410 doi:10.1029/2011JB008253.
411 Masson, D., C. Harbitz, R. Wynn, G. Pedersen, and F. Løvholt, 2006, Submarine landslides—Processes,
412 triggers and hazard prediction, Philos. Trans. R. Soc. A., 364, 2009–2039.
413 Matsumoto, H., T. Baba, K. Kashiwase, T. Mitsu, and Y. Kaneda, 2012, Discovery of Submarine
414 landslide Evidence Due to the 2009 Suruga Bay Earthquake, in Submarine mass movements and
415 their consequences edited by Y. Yamada et al., Advances in Natural and Technological Hazards
416 Research, 31, 549–559.
417 Matsumoto, T., M. Kimura, 1993, Detailed Bathymetric Survey in the Sea Region of the Estimated
418 Source Area of the 1771 Yaeyama Earthquake Tsunami and Consideration of the Mechanism of Its
419 Occurrence, Zisin 2, 45, 417-426 (in Japanese with English abstract).
420 McLeod, P., S. Carey, and R. S. J. Sparks (1999), Behaviour of particle-driven flows into the ocean:
421 Experimental simulation and geological implications, Sedimentology, 46, 523–536,
422 doi:10.1046/j.1365-3091.1999.00229.x.
423 Moore, G.F., and M. Stasser, 2016, Large mass transport deposits in Kumano basin, Nankai trough,
424 Japan, in Submarine mass movements and their consequences edited by G. Lamarche et al.,
425 Advances in Natural and Technological Hazards Research, 41, 371-380.
426 Moriki, H., T. Kumamoto, T. Nakata, H. Goto, N. Izumi, A. Nishizawa, 2017, Identification of landslide
427 and its characteristics on the seafloor around Japan using anaglyph images, Report of hydrographic
428 and oceanographic researches, 54, 1-16 (in Japanese with English abstract).
429 Muhari, A., F. Imamura, T. Arikawa, A. Hakim, and B. Afriyanto, 2018, Solving the Puzzle of the
430 September 2018 Palu, Indonesia, Tsunami Mystery: Clues from the Tsunami Waveform and the
431 Initial Field Survey Data, J. Disaster Res., 13, sc20181108.
432 Saito T., 2013, Dynamic tsunami generation due to sea-bottom deformation: Analytical representation
433 based on liner potential theory, Earth Planets Space, 65, 1411-1423, doi:10.5047/eps.2013.07.004.
434 Saito T., 2019, Tsunami generation and propagation, 265pp. Springer Geophysics,
435 https://doi.org/10.1007/978-4-431-56850-6_1.
436 Sassa, S., and T. Takagawa, 2018, Liquefied gravity flow-induced tsunami: first evidence and

comparison from the 2018 Indonesia Sulawesi earthquake and tsunami disasters, Landslides, doi:https://doi.org/10.1007/s10346-018-1114-x.

Satake, K., 2007, Volcanic origin of the 1741 Oshima-Oshima tsunami in the Japan Sea, Earth Planet. Sp., 59, 381–390.

Strasser, M., G.F. Moore, G. Kimura, A.J. Kopf, M.B. Underwood, J. Guo, E.J. Screaton, 2011, Slumping and mass transport deposition in the Nankai fore arc: Evidence from IODP drilling and 3-D reflection seismic data, Geochemistry Geophysics, Geosystem, 12, doi:10.1029/2010GC003431.

Strasser, M., P. Henry, T. Kanamatsu, M.K. Thu, G.F. Moore, and IODP Expedition 333 Scientists, 2012, Scientific drilling of mass-transport deposits in the Nankai accretionary wedge: first results from IODP expedition 333, in Submarine mass movements and their consequences edited by Y. Yamada et al., Advances in Natural and Technological Hazards Research, 31, 671-681.

Tappin, D.R., P. Watts, G.M. McMurtry, Y. Lafoy, T. Matsumoto, 2001, The Sissano, Papua New Guinea tsunami of July 1998 – offshore evidence on the source mechanism, Marine Geology, 175, 1-23.

Tappin, D.R., P. Watts, S.T. Grilli, 2008, The Papua New Guinea tsunami of 17 July 1998: anatomy of a catastrophic event, Nat. Hazards Earth Syst. Sci., 8, 243–266.

Tappin, D.R., S.T. Grilli, J.C. Harris, R.J. Geller, T. Masterlark, J.T. Kirby, F. Shi, G. Ma, K.K.S. Thingbaijam, P.M. Mai, 2014, Did a submarine landslide contribute to the 2011 Tohoku tsunami?, Marine Geology, 357, 344–361, doi:10.1016/j.margeo.2014.09.043.

Watada, S., 2013, Tsunami speed variations in density-stratified compressive global oceans, Geophys. Res. Lett., 40, 4001-4006, doi:10.1002/grl.50785.

Watts, P., S.T. Grilli, D.R. Tappin, and G.J. Fryer, 2005, Tsunami Generation by Submarine Mass Failure. II: Preditive Equations and Case Studies, Journal of Waterway, Port, Coastal, and Ocean Engineering, 298-310.

Yamada, Y., Y. Yamashita, and Y. Yamamoto, 2010, Submarine landslides at subduction margins: Insights from physical models, Tectonophysics, 484, 156–167.

Yamamoto, Y., and S. Kawakami, 2014, Along-strike migration of intermittent submarine slope failures at subduction margins: Geological evidence from the Chikura group, Central Japan, in Submarine Mass Movements and Their Consequences edited by S. Krastel et al., Advances in Natural and Technological Hazards Research, 37, 551-560, doi:10.1007/978-3-319-00972-8_49.

Yanagisawa, H., Goto, K., Sugawara D., K. Kanamaru, N. Iwamoto, Y. Takamori, 2016, Tsunami earthquake can occur elsewhere along the Japan Trench - Historical and geological evidence for the 1677 earthquake and tsunami -, J. Geophy. Res., 121, 3504–3516, doi:10.1002/2015JB012617.

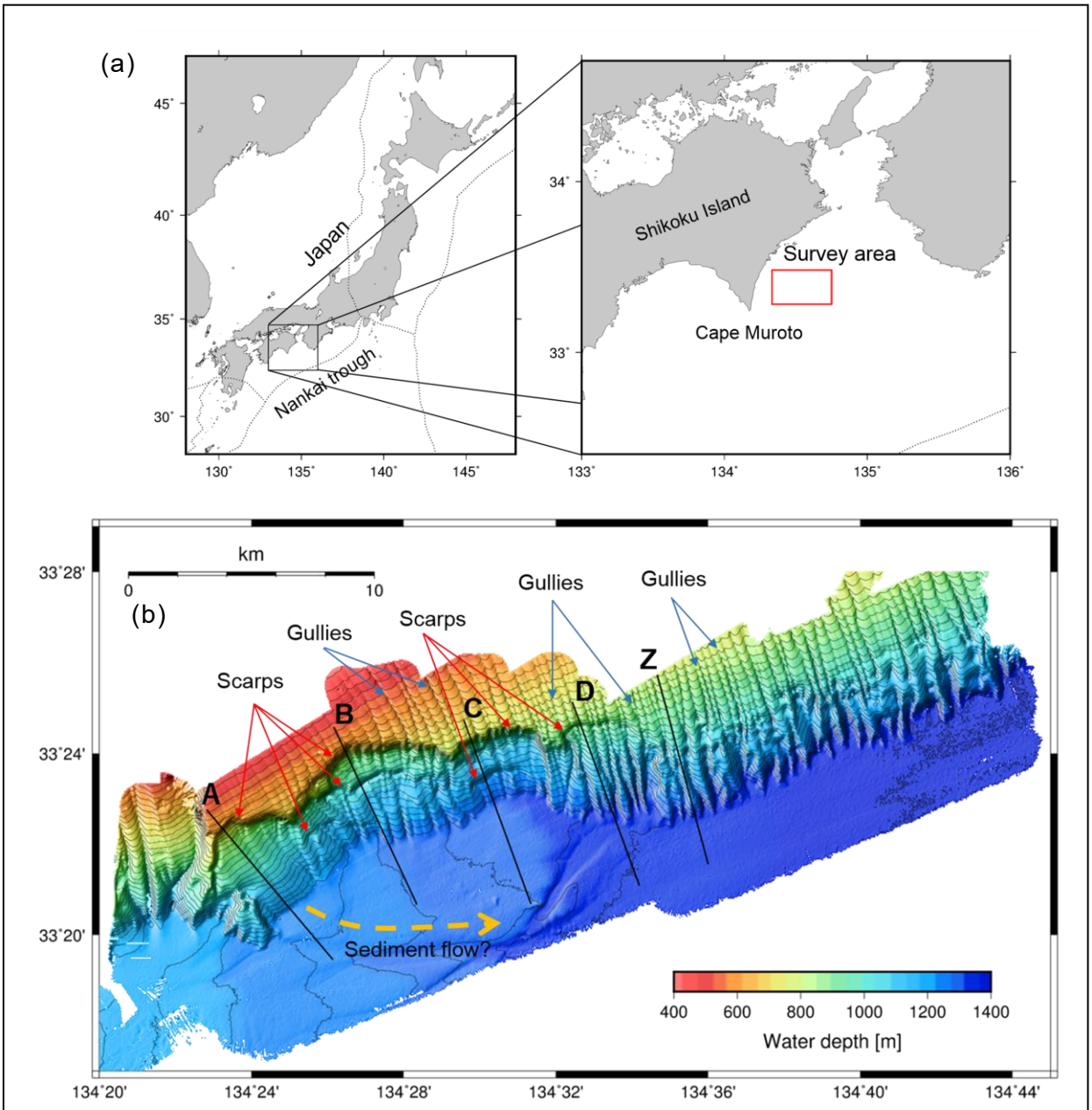

Fig. 1. (a) Location map of Japan showing the bathymetric survey area within the red rectangle. Dotted lines are the plate boundaries from Bird (2003). (b) Bathymetry of submarine slump scarps in the study area. Contour interval is 25 m. Horizontal data resolution (horizontal interval between data points) is about 50 m. Thin black lines A–D and Z are profiles shown in Fig. 2.

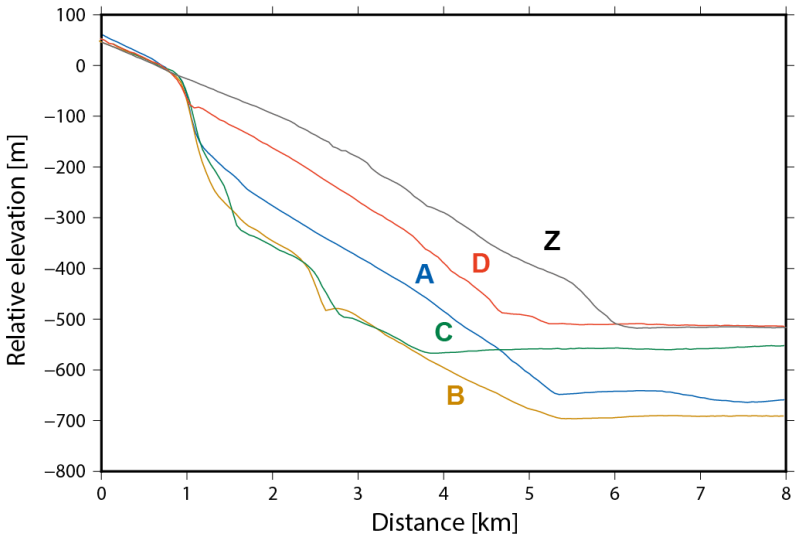

Fig. 2. Bathymetric (relative depth) profiles along the profile lines shown in Fig. 1b. The zero level in the vertical axis is the water depth at the headscarps.

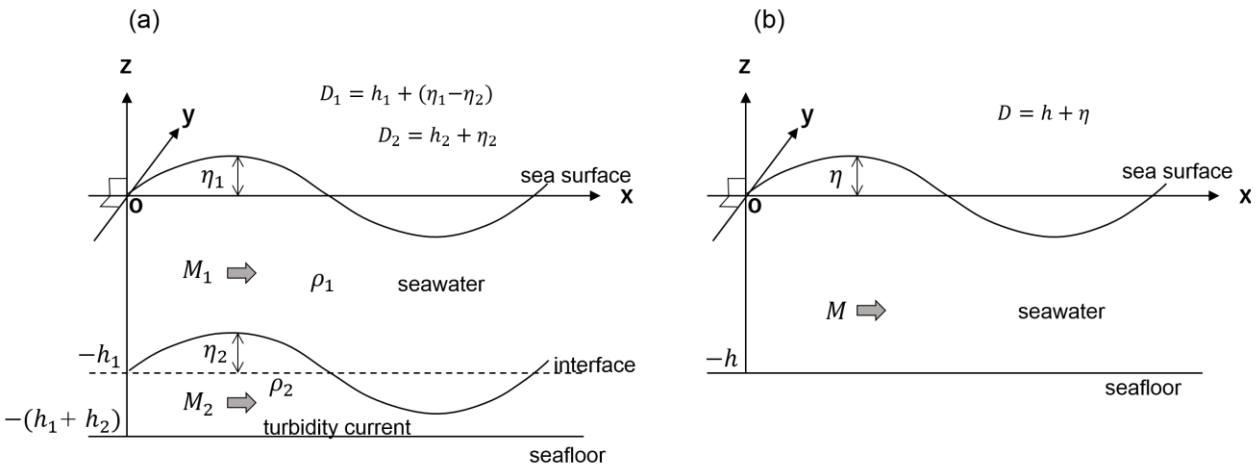

Fig. 3. Schematic diagrams showing the notation of (a) the two-layer flow model for equations (1)–(6), and (b) the one-layer flow model for equations (7)–(13).

482
483

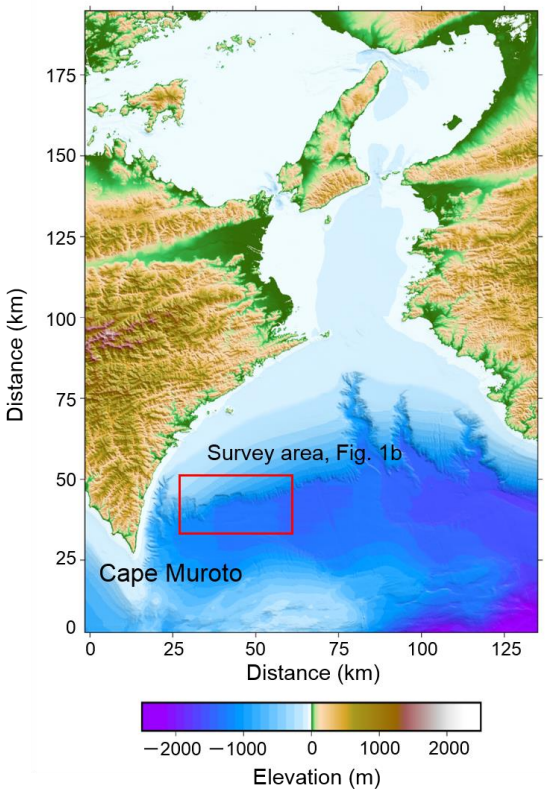

Fig. 4 Computational domain for modeling of submarine landslide and tsunamis

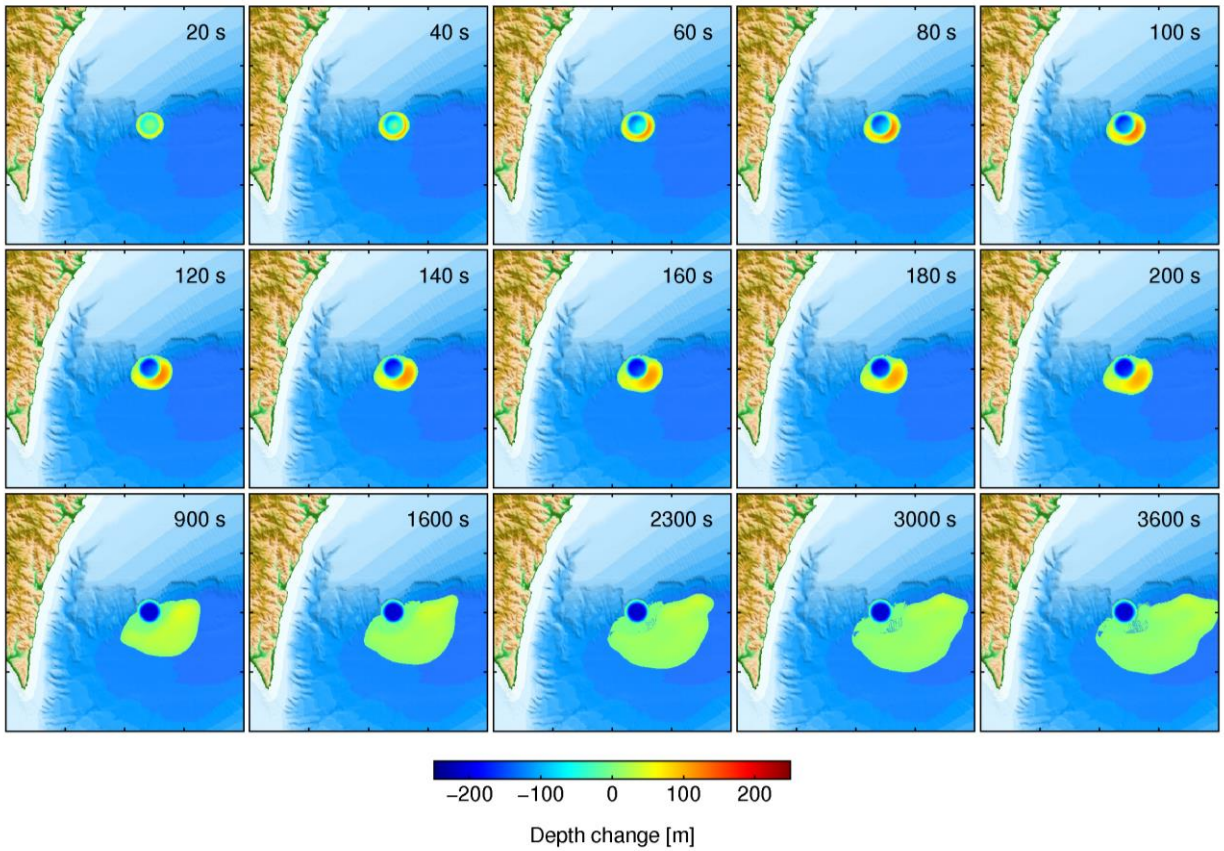

Fig. 5. Changes in water depth due to the simulated submarine mass movements from 20 to 3,600 s after the collapse initiation. Negative (blue) and positive (red) depth changes indicate erosion and deposition relative to the initial bathymetry, respectively.

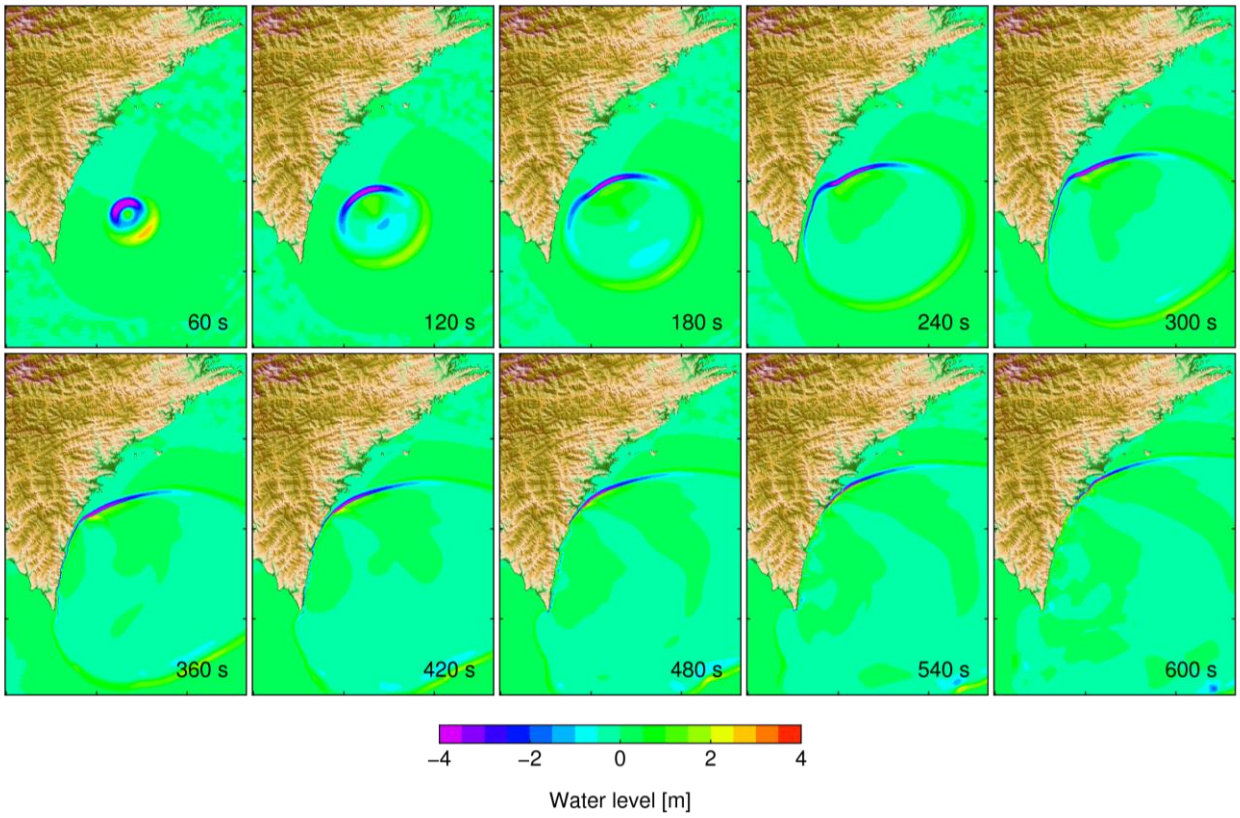

Fig. 6. Submarine landslide tsunami from 60 to 600 s calculated by shallow water equations without dispersion terms.

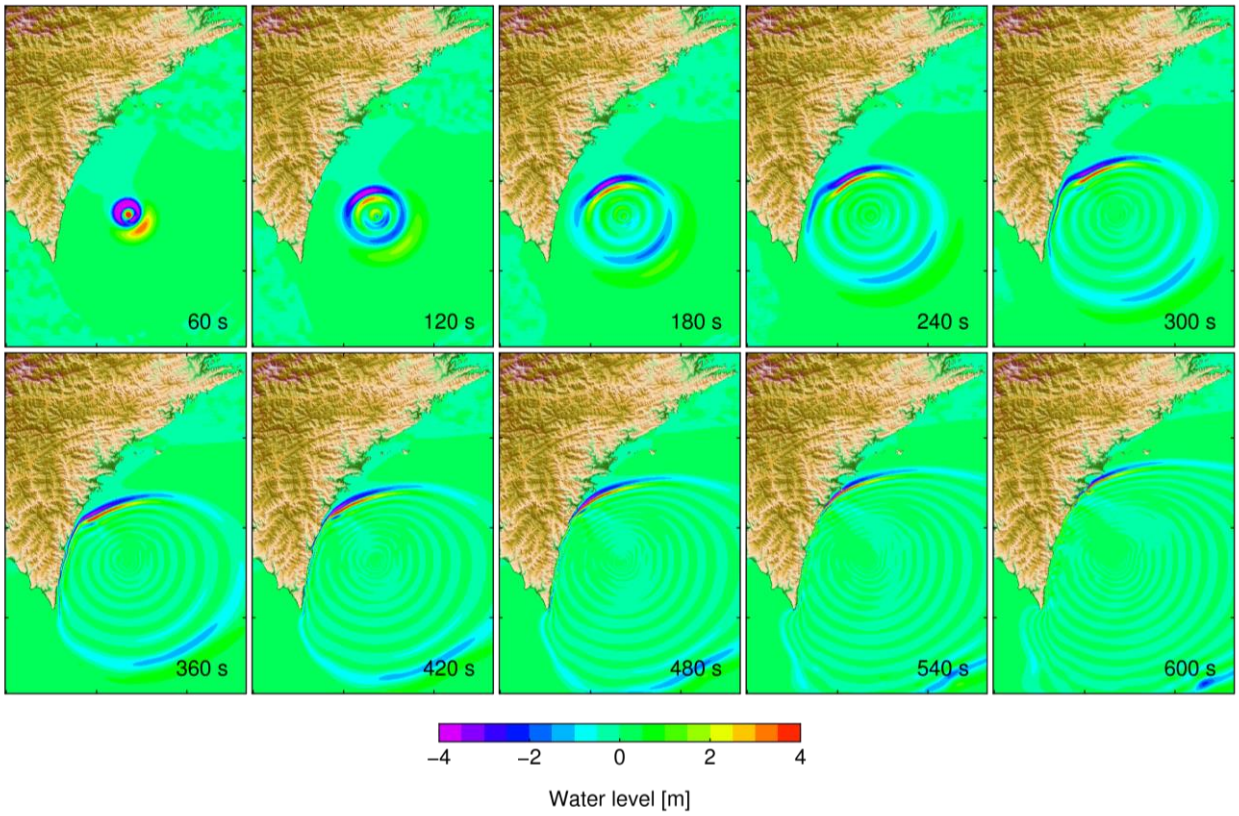

Fig. 7. Submarine landslide tsunami from 60 to 600 s calculated by shallow water equations with dispersion terms

524

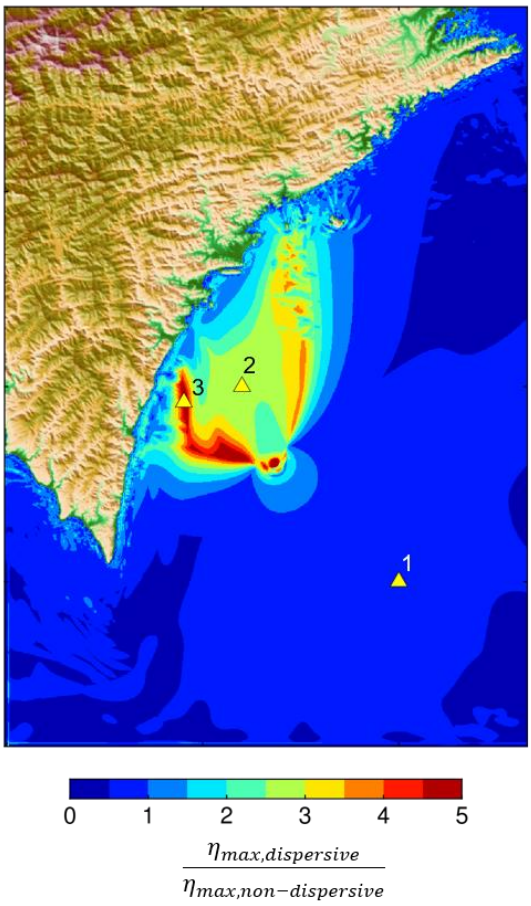

Fig. 8. Ratio of maximum tsunami heights calculated by shallow water equations with dispersion terms to those calculated without dispersion terms. Triangles indicate locations of imaginary gauges corresponding to simulated waveforms shown in Fig. 9.

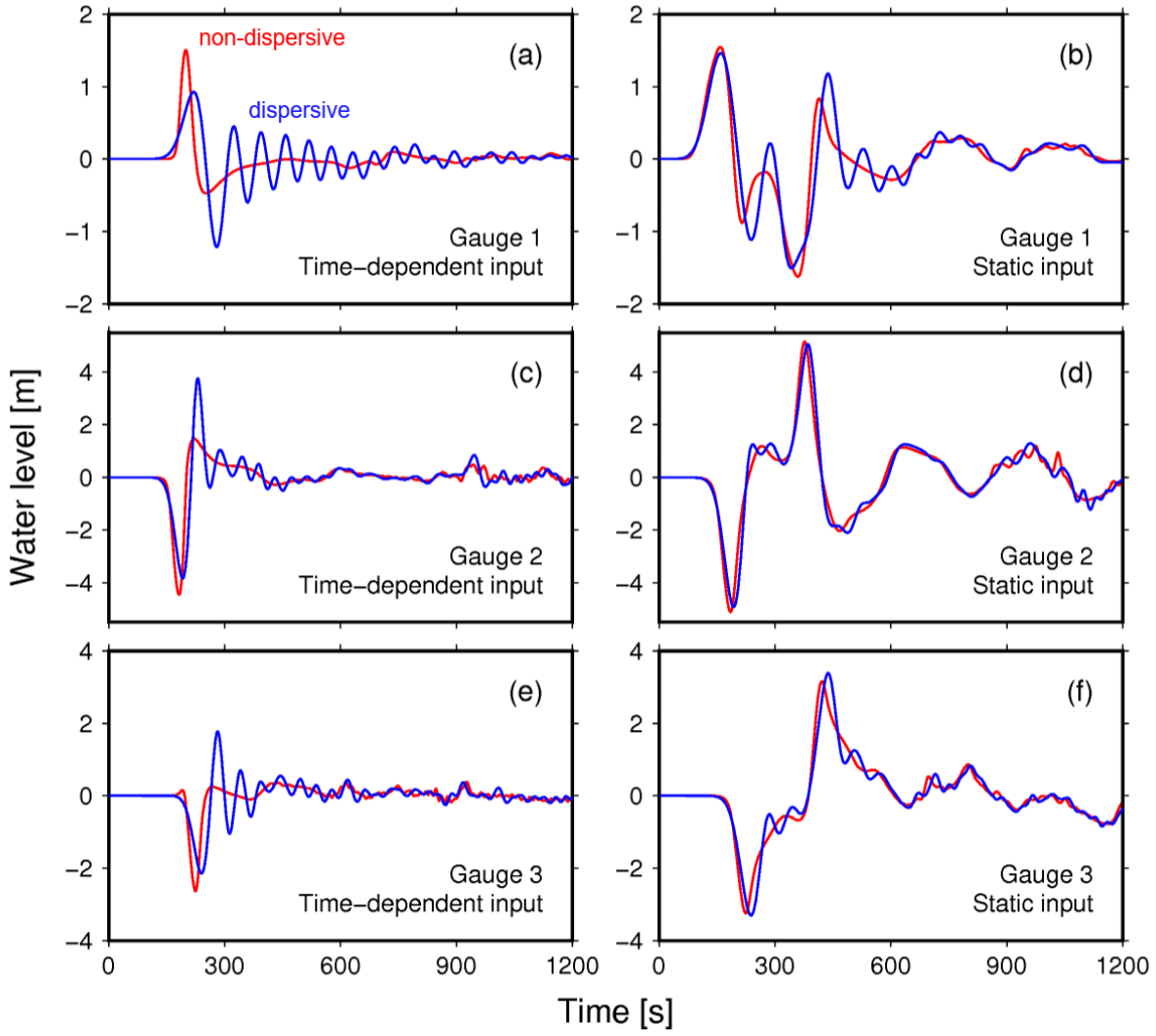

Fig 9. Calculated tsunami waveforms for the three imaginary gauges shown in Fig. 8. Red curves are calculated without dispersion terms and blue curves are calculated with dispersion terms. Left-hand panels (a, c, and e) and right-hand panels (b, d, and f) are calculated with time-dependent and static inputs, respectively.

Table 1. Slump parameters

Slump (Fig. 2)	A	B	C	D
Water depth of headscarp	660 m	640 m	760 m	850 m
Headscarp width (km)	4.2 km	6.9 km	3.7 km	3.2 km
Length (km)	4.2 km	4.2 km	2.7 km	2.9 km
Estimated thickness	210 m	280 m	280 m	90 m
Slope angle	7°	5°	4°	6°
Estimated volume	1.9 km^3	4.8 km^3	1.3 km^3	0.4 km^3